Åström, Jan; Polojärvi, A.

High-Resolution Fracture Dynamics Simulation of Pack-Ice and Drift-Ice Formation During Sea Ice Break up Events Using the HiDEM2.0 Code

Published in:
Geophysical Research Letters

DOI:
10.1029/2024GL110552

Published: 28/09/2024

Document Version
Publisher's PDF, also known as Version of record

Geophysical Research Letters®

RESEARCH LETTER
10.1029/2024GL110552

Key Points:

- Ultra high-definition simulation (0.5 m elements) of sea ice fragmentation on a square kilometer scale
- The HiDEM model captures in fine detail the formations of leads, pressure ridge networks, and floe-size distributions
- The model reveals features that cannot be reproduced by rheological models, suggesting a hybrid method for prediction

Correspondence to:
J. A. Åström,
astrom@csc.fi

Citation:
Åström, J. A., & Polojärvi, A. (2024). High-resolution fracture dynamics simulation of pack-ice and drift-ice formation during sea ice break up events using the HiDEM2.0 code. *Geophysical Research Letters*, *51*, e2024GL110552. https://doi.org/10.1029/2024GL110552

Received 3 JUN 2024
Accepted 11 SEP 2024

Author Contribution:
Conceptualization: J. A. Åström
Formal analysis: J. A. Åström
Investigation: J. A. Åström
Methodology: J. A. Åström
Software: J. A. Åström
Validation: J. A. Åström
Visualization: J. A. Åström
Writing – original draft: J. A. Åström
Writing – review & editing: J. A. Åström

High-Resolution Fracture Dynamics Simulation of Pack-Ice and Drift-Ice Formation During Sea Ice Break up Events Using the HiDEM2.0 Code

J. A. Åström[1] and A. Polojärvi[2]

[1]CSC—It Center for Science Ltd., Espoo, Finland, [2]Department of Mechanical Engineering, Aalto University, School of Engineering, Aalto, Finland

Abstract Creating accurate predictive models for drift and pack ice is crucial for a wide array of applications, from improving maritime operations to improving weather prediction and climate simulations. Traditional large-scale sea ice dynamics models rely on phenomenological ice rheology to simulate ice movements. These models are efficient on large scales but struggle to depict smaller-scale ice features. In our study, we use a new version of the HiDEM discrete element model software to examine the formation of drift and pack ice under various stress conditions. Our findings show that high-resolution size distributions of ice floes are universal and multimodal, and that compression ridges form three distinct zones. Reproducing complex characteristics of this nature in a standard rheology model is challenging, suggesting that a combination of models may be necessary for more precise predictions of sea ice dynamics. We propose a potential hybrid algorithm that integrates these approaches.

Plain Language Summary Sea ice forms in cold climates and is susceptible to being easily fragmented by wind and currents, resulting in a dynamic landscape comprising solid fast ice, drift ice and pack ice. Pack ice, in particular, can pose challenges such as hindering shipping, causing damage to offshore structures, and complicating traditional fishing and hunting activities. Operational models for sea ice dynamics are currently utilized to optimize ship routes and the deployment of icebreakers. Although existing rheology-based models perform well on large scales, they encounter difficulties in capturing the finer details that are often crucial. In this study, we utilize a high-resolution Discrete Element Model computer code that is capable of simulating detailed sea ice dynamics at scales ranging from meters to kilometers. Our simulation results reveal insights that are not readily obtained from conventional large-scale models, and we explore the potential for integrating these two approaches to create a hybrid model.

1. Introduction

Sea ice plays a crucial role in climate and weather systems. Its high albedo, compared to ice-free waters, significantly affects the climate. Changes in sea ice can indirectly disrupt normal ocean circulations. Dense and deformed sea ice has consistently created challenges for shipping and offshore infrastructure. For Arctic indigenous peoples, any changes in sea ice are potentially problematic as they rely on land-fast ice for travel. To address these issues, a comprehensive understanding of sea ice dynamics at various scales is necessary, from meter-scale ice failure events against offshore structures to large-scale drift and pack ice movements spanning thousands of kilometers in the Arctic Ocean.

In computational models, sea ice is often represented as a continuum in the form of differential equations. These models are frequently used on spatial scales greater than kilometers due to their computational efficiency and applicability over large areas and extended periods. However, a major challenge persists in defining an appropriate rheology for sea ice, with no consensus on the best method. A pioneering work in this field was the creation of the visco-plastic model by Hibler, 1977, 1979, which remains widely adopted in various forms. While this model captures many aspects of large-scale ice dynamics, it fails to represent small-scale features such as leads, ridges, shear zones, and floe fields. Other continuum models include the elastic-decohesive model proposed by Schreyer et al. (2006), the Maxwell elasto-brittle model introduced by Dansereau et al. (2016), and the brittle Bingham-Maxwell rheology model by Ólason et al. (2022). Modern high-resolution continuum models have shown the capability to replicate observed large-scale fracturing (Bouchat et al., 2022; Hutter et al., 2022), with some models having grid resolutions of a few kilometers (Kärnä et al., 2021; Pemberton et al., 2017; Röhrs et al., 2023), but even the most advanced continuum models struggle to represent the formation of leads and ridges. This limitation affects their predictive power and highlights the need for complementary approaches in computational ice dynamics (Blockley, 2020; Feltham, 2008).

Compared to the continuum approach, Discrete Element Models (DEM) represent a different type of algorithm (Cundall & Strack, 1979). In DEM, numerous discrete elements (DEs) are initially connected by interaction potentials, which can be depicted as, for example, beams or springs, to form intact sea ice. During simulations, these interactions can reach fracture thresholds, causing the connections between DEs to break and the ice to fragment into discrete floes. These floes can further fail due to interactions with both intact ice and other ice floes. This explicit method of describing ice failure and fragmentation contrasts sharply with the differential equation approach used in continuum models.

Initial DEMs for sea ice utilized circular DEs moving in two dimensions (Babic et al., 1990; Hopkins & Hibler, 1991). Soon after, two-dimensional DEM with polygonal DEs was used to study pressure ridge formation (Hopkins, 1994, 1998; Hopkins et al., 1991, 1999). Additionally, Hopkins et al. (2004) and Hopkins and Thorndike (2006) modeled Arctic pack ice in 2D, where ridge formation at floe-to-floe contacts was described using a contact interaction model developed by Hopkins (1996). Although the details of ice deformation were not specified, the study demonstrated the effectiveness of using DEM to describe large-scale sea ice dynamics. A similar approach was later employed by West et al. (2022) to simulate ice dynamics in the Nares Strait and by Herman (2022) to investigate the applicability of granular rheologies on densely packed ice floe fields. Manucharyan and Montemuro (2022) recently introduced a two-dimensional tool where the DEs had evolving shapes, based on a basic failure model depicting sea ice failure. Advances in high-performance computing now allow for explicit three-dimensional modeling of ice dynamics at the 5-10 m-scale resolution over large sea areas (J. Åström et al., 2024). This enables the representation of individual ice floes, ridges, and leads in large-scale sea ice simulations. A major advantage is that the simulations produce ice fragments, most of which consist of numerous DEs. This facilitates the spontaneous development of ice floe size distributions that accurately reflect the fragmentation processes.

In this research, we utilize a novel GPU-accelerated version of the HiDEM code to model sea ice dynamics at a high-detail resolution of half a meter. We use the model in a set of loading experiments to explore the universal fragment size distributions described in Section 2.2.

2. Methods

2.1. Discrete Element Model

The HiDEM code models the behavior of elastic, inelastic, and breakable bodies through interconnected DEs as previously described. These DEs move according to Newton's laws of motion, incorporating energy dissipating factors such as friction, drag, and inelasticity. The connections between DEs, represented as beams in HiDEM, are established during the setup phase, and these beams break when subjected to stresses exceeding the material's allowable stress state. A major challenge in creating an effective DEM is to implement both precise DE interactions and use a high resolution (or small DEs), which combined demand substantial computational resources. This challenge is compounded by the fact that many modeled materials have high stiffness and low mass density, resulting in high sound velocity, fast-moving stress waves, and high crack propagation velocity. This necessitates the use of small time steps in computations to prevent modeling instabilities. Consequently, DEMs requires the development of highly optimized computer codes that can efficiently utilize modern high-performance computers. HiDEM has been specifically designed to address these challenges. It is parallelized using two methods: MPI for inter-node communication and OpenMP for intra-node multithreading on multi-core CPUs. Alternatively, the code can be compiled with MPI for CPUs and offload intensive computations to GPUs using CUDA or HIP computer languages. This coding structure introduces complexity, necessitating meticulous optimization to overcome computational bottlenecks and load imbalances. The simulations in this study were conducted on the EuroHPC supercomputer LUMI in Kajaani, Finland. LUMI's computing power primarily relies on 10,240 AMD Radeon Instinct MI250X GPUs, with a theoretical peak performance exceeding 550 petaflops. It is noteworthy that the simulations here only utilized 2–4 nodes, running for a 0.5–2 hr per simulation, which would allow for a significant increase in both size and duration of future simulations. The HiDEM code was initially designed to study brittle fragmentation from a statistical physics perspective. An early overview of the findings can be found in J. A. J. A. Åström (2006). HiDEM has since been used in simulations for mining blasts (Iravani et al., 2018), glacier calving (Benn & Åström, 2018), ice shelf fracturing (Benn et al., 2022), and sea ice failure and deformation on various scales (Prasanna et al., 2022; J. Åström et al., 2024).

HiDEM features a straightforward design aimed at high-resolution large-scale simulations. The intact ice is described by spherical DEs interconnected by elastic-brittle Euler-Bernoulli beams. DEs interact through connecting beams or collision forces. By defining the position vector, $\vec{x}_i$, of DE i, which encompasses translational and rotational degrees of freedom, the DEM equations of motion can be formulated as:

$$m_i \ddot{\vec{x}}_i + \sum_j K \vec{x}_{ij} + \sum_j C_2 \dot{\vec{x}}_{ij} + C_1 \dot{\vec{x}}_i = \vec{F}_i, \tag{1}$$

where m_i represents the mass or moment of inertia of DE i, C_1 denotes drag coefficients encompassing water, air, and land-friction drag, $\vec{F}_i$ denotes external forces and moments such as gravity and buoyancy. Moreover, $K = K(t)$ and C_2 denote components of contact-stiffness, beam-stiffness, and damping matrices for the interaction between discrete elements i and j, while $\vec{x}_{ij}$ indicates the position vector between object i and its neighboring object j. The terms $\ddot{\vec{x}}$ and $\dot{\vec{x}}$ correspond to the second- and first-order time derivatives of $\vec{x}$.

In this study, sea ice is formed by arranging DEs into a thin sheet composed of tightly packed spheres in an HCP lattice configuration. For the boundary conditions, we either apply free conditions, enabling DEs to move out of the original domain without restriction, or fixed conditions, which confine DEs attempting to exit the domain at the boundary. We use simple linear drag with different constants for water, air and land. Our model simplifies water drag significantly. This approach is taken because DEs encounter varying levels of drag depending on whether they are situated on the ice floe's edges, their position relative to the floe's movement, or the density of the surrounding melange. Accurately identifying these diverse drag forces is computationally too intensive, so we opted for a simplified yet effective method.

2.2. Universal Fragment Size Distributions

When exposed to strong external forces, intact sea ice undergoes a fragmentation process. Simulating this fragmentation process is complex yet crucial for comprehending the dynamics of sea ice. Specifically, it requires both high spatial and temporal resolutions over extensive regions. While each fragmentation event is distinct, they exhibit common statistical characteristics. Consequently, fragmentation processes are most accurately represented by a set of functions that can be integrated to create distribution functions for fragment sizes, clarifying the outcomes of fragmentation processes under different loading conditions.

Several key principles influence the development of Fragment Size Distributions (FSDs) resulting from the fracturing of brittle materials (see: J. A. J. A. Åström (2006) for a review). (a) Branching and merging of propagating cracks result in power-law FSDs, typically showing an exponential cut-off at larger sizes. In this context, the power exponent is universally expressed as $-(2D-1)/D$, where D is the Euclidean dimension of the fragmenting object. (b) Crushing and grinding of already fragmented material under compression or compressive shear cause further fragmentation, a reduction in the power exponent, and the compaction of the material. (c) Random and uncorrelated formation of more or less straight cracks leads to exponential FSDs.

The branching and merging of cracks, as denoted in (a), manifest in brittle materials when propagating cracks become unstable and generate crack branches. These crack branches tend to merge as the tensile stress at a crack tip becomes oriented toward existing cracks in the vicinity. Essentially, the resulting FSD can be explained as follows: as crack branches merge pairwise, only half of them persist after each merging event. The remaining crack branches are spaced further apart and consequently form larger fragments away from the main crack. This leads to the formation of fragmentation zones within the material, rather than simple linear crack structures. The power exponent value, which is -1.5 for two-dimensional features, such as sea ice on large enough scale, originates from the fact that the number of fragments formed in each generation, N, of crack branching-merging scales as $(1/2)^N$, while their sizes scale as 2^{2N}. This results in an FSD, $n(s)$, describing the number density of fragments of size s, following the form $n(s)ds' \propto s^{-0.5}$, where ds' denotes the change in fragment size between two generations of merging crack-branches. This oversimplified model assumes a discrete set of fragment sizes. Substituting ds' with a constant ds for a continuous function reduces the exponent to -1.5. Crack branches propagating away from the main crack will eventually come to a halt, often leading to an exponential 'cut-off' at a characteristic size, s_0. This results into a FSD of the form

$$n(s) \propto s^{-1.5} \exp\left(-(s/s_0)^{\delta}\right), \tag{2}$$

where δ is a dimensional factor, taking values of 1 or 0.5 depending on whether the cut-off is proportional to the linear size of fragments or their areas.

The generation of FSDs through crushing and grinding, as mentioned in (b), is a compaction mechanism. When a field of pack-ice breaks under compression or compressive shear, the highest stresses usually occur near voids, leading to local fragmentation and subsequent compaction. This compaction mechanism can be described, for example, by variations of Apollonian packings (Manna & Herrmann, 1991). Processes of this kind result in dense packings, all producing power-law FSDs with characteristic exponents. A fragmentation-driven compaction process reduces fragment sizes by breaking larger fragments into smaller ones, suggesting that crushing and grinding of pack-ice lead to power-law FSDs with smaller exponents compared to initial breakups often described by the crack-branching process.

The FSDs produced by process (c) correspond to a two-dimensional Poisson process. Fragmentation of this type was studied by Grady and Kipp (1985). The FSD can be an exponential function of either the fragment area or the fragment length.

3. Sea Ice Simulations

We employ the HiDEM code to model sea ice dynamics and fragmentation with a high resolution that allows for the precise representation of ridge and lead formation, as well as the distribution of fragment sizes, across varying loading scenarios to show that the model reproduces the theoretically expected behavior laid out in Section 2.2.

This section describes simulations in which intact ice, ranging in area from 1 to 4 km^2 and having a thickness of 1m, fail under shear, tension, compression, or interactions with land. The forcing is induced by loads that mimic wind or currents. However, typical metocean forces are generally inadequate to fracture sea ice of this size; hence, the applied loads are approximately an order of magnitude greater than those naturally occurring.

3.1. Ice Failure Due to Shear

Figure 1 shows the result for a sea ice square, $x \in [0m : 1000m], y \in [0m : 1000m]$, that is fragmented by pure shear. The force components on individual DEs are given by:

$$\begin{aligned} F_x &= f(y - 500) \\ F_y &= f(x - 500), \end{aligned} \tag{3}$$

where f is scale factor for the force.

The simulation results with $f = 0.2$ are represented in Figures 1a and 1b, while Figures 1c and 1d show the results with $f = 0.3$. In the case $f = 0.2$, a single large lead is formed perpendicular to the direction of maximum tensile stress Figure 1b, with a large set of floes forming within the lead. The FSD for this case is shown in Figure 1a. The distribution function for the smaller floes within the lead is well described by (a) and Equation 2, with an exponential cut-off at $s_0 \approx 1600$, in units of DEs. In addition to this crack-branching function, there is a residue of a few larger floes, including the two unbroken large ice areas on both sides of the lead. For $f = 0.3$ the ice shatters completely (Figure 1d). The FSD is well described by two crack-branching functions at two different scales: one for floes below $s < 300$, and another $s < 50000$. The floes typically have a large aspect ratio in both cases. A published image where this kind of floe formation can be observed is, for example, Figure 1b in Rheinlænder et al. (2022), representing a breakup event in the Beaufort sea in 2013.

3.2. Ice Failure Under Tension

The next case is the same square ice floe as in the previous case, this time broken by isotropic tension

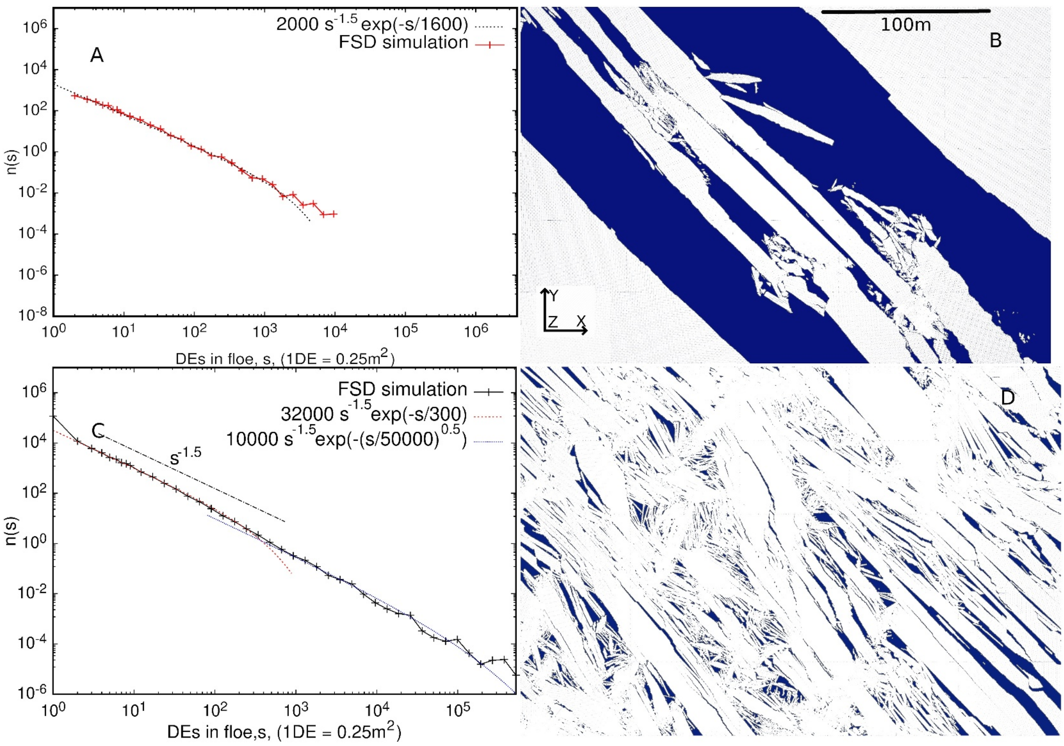

Figure 1. (a) The FSD of a square kilometer 1m thick sea ice under pure shear stress with $f = 0.2$. Equation 2 is fitted to the simulation data. (b) A snapshot of the fragmented ice. A single large lead has formed perpendicular to tensile direction, and a lot of floes have formed within the lead. (c) The FSD with $f = 0.3$. Equation 2 is fitted to the data, separately for two different size ranges. (d) Snapshot of shattered sea ice under strong load. Ice is white, water is dark blue.

$$
\begin{aligned}
F_x &= f(x - 500) \\
F_y &= f(y - 500),
\end{aligned}
\tag{4}
$$

with $f = 0.1$. Figure 2b shows the result of this exercise. The tensile stress induce a set of major leads that divide the ice into a set of large ice floes. Within the leads a number of small floes appear. Figure 2a shows the FSD, which has the small floes described by the crack-branch function Equation 2, whereas the large floes are described

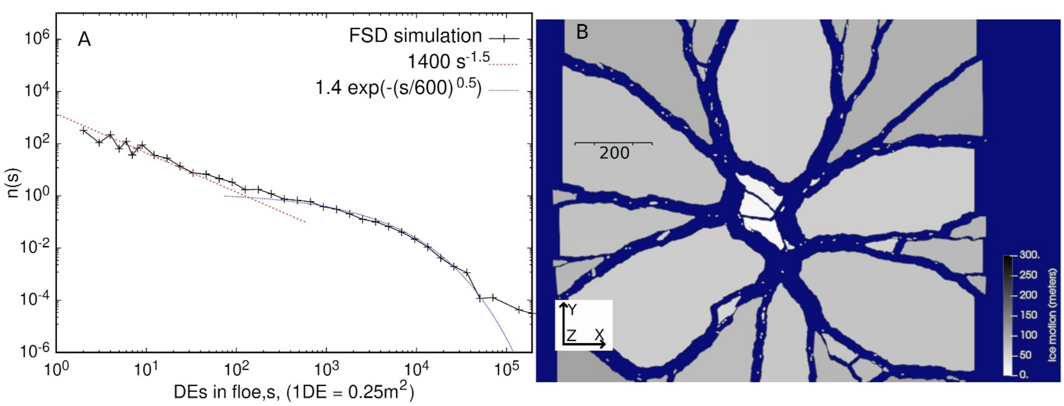

Figure 2. (a) The FSD of a square kilometer 1m thick sea ice under symmetric tension. This FSD is a combination of *(1)* and *(3)* (b) A snapshot of the fragmented ice. The color code represent ice motion during the 5 min simulation. Water is dark blue, ice is represented by the gray scale.

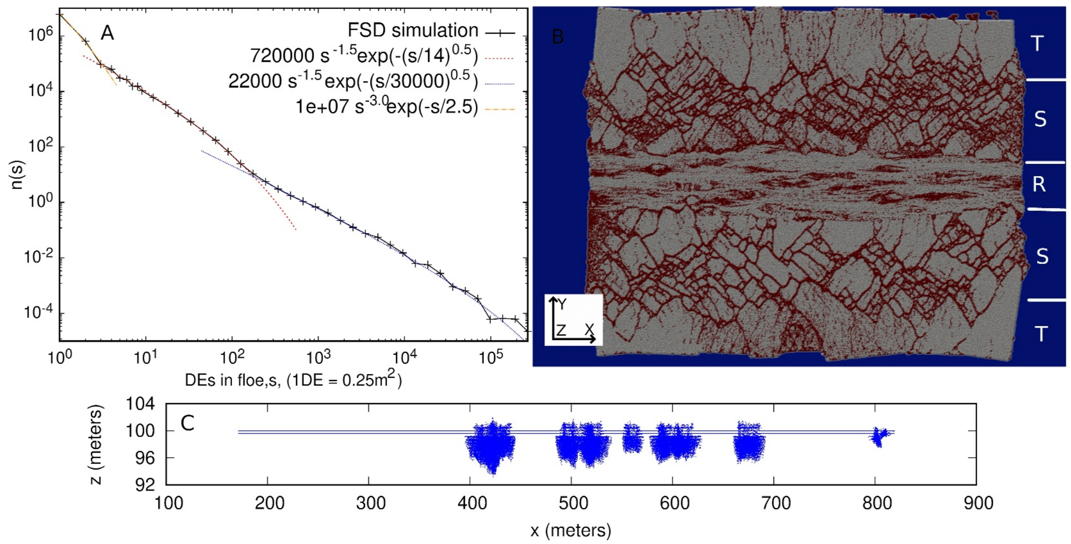

Figure 3. (a) The FSD of a square kilometer 1m thick ice fragmented under uni-directional compression. (b) Ice fragments with less than 100 DEs. These fragments make up a network of compression ridges in regions marked 'R' and 'S', formed via out-of-plane and in-plane shear deformations, and tensile leads in 'T'. (c) A cross-sectional view of the ice for a narrow strip in the middle of the domain, illustrating the ridges.

by an exponential function corresponding to (c). Similarly to the previous case, the FSD again shows a residual of a few very large floes.

3.3. Ice Failure Under Compression

The third case is a uni-directional compression where

$$\begin{aligned} F_x &= 0 \\ F_y &= -f(y-500), \end{aligned} \tag{5}$$

with $f = 0.3$.

For this case the failure pattern is more complex than the two previous. Figure 3b display all resulting small ice fragments, with less than 100 DEs. The fragments are concentrated in compression ridges and, to a smaller extent, within leads formed under tension farthest away from the highest compression at the center in the y-direction. This figure also displays three distinct regimes marked with 'R', 'S' and 'T'. In the 'R' region, high compressive stress breaks the ice via out-of-plane shear, with some similarities to buckling, and compression ridges are formed perpendicular to the compression direction. The formation of these ridges allows the stress symmetry to be broken and ridges diagonal to the y-direction form as a result of in-plane shear stress in the regions marked "S". Finally, distances farthest from the compression center dilation in the x-direction allow tensile leads to form parallel to the stress direction. Here fracture-induced leads dominate in contrast to ridges as in the other two regimes. Ridge structures of this kind can be observed, for example, close to a shore lines when ice is pressed against it (Marbouti et al., 2020).

For this case, the FSD can again be described as two crack-branching functions that terminate in exponential cut-offs at different sizes: $s_0 = 14$, and $s_0 = 30000$. For the very smallest fragments, ($s = 1,2$), there may be a third size regime, but for such small floes discretization likely plays a significant role and this may be just a model artifact. This case again correspond to (a), except for the very smallest fragments which may be a result of fragmentation process (b).

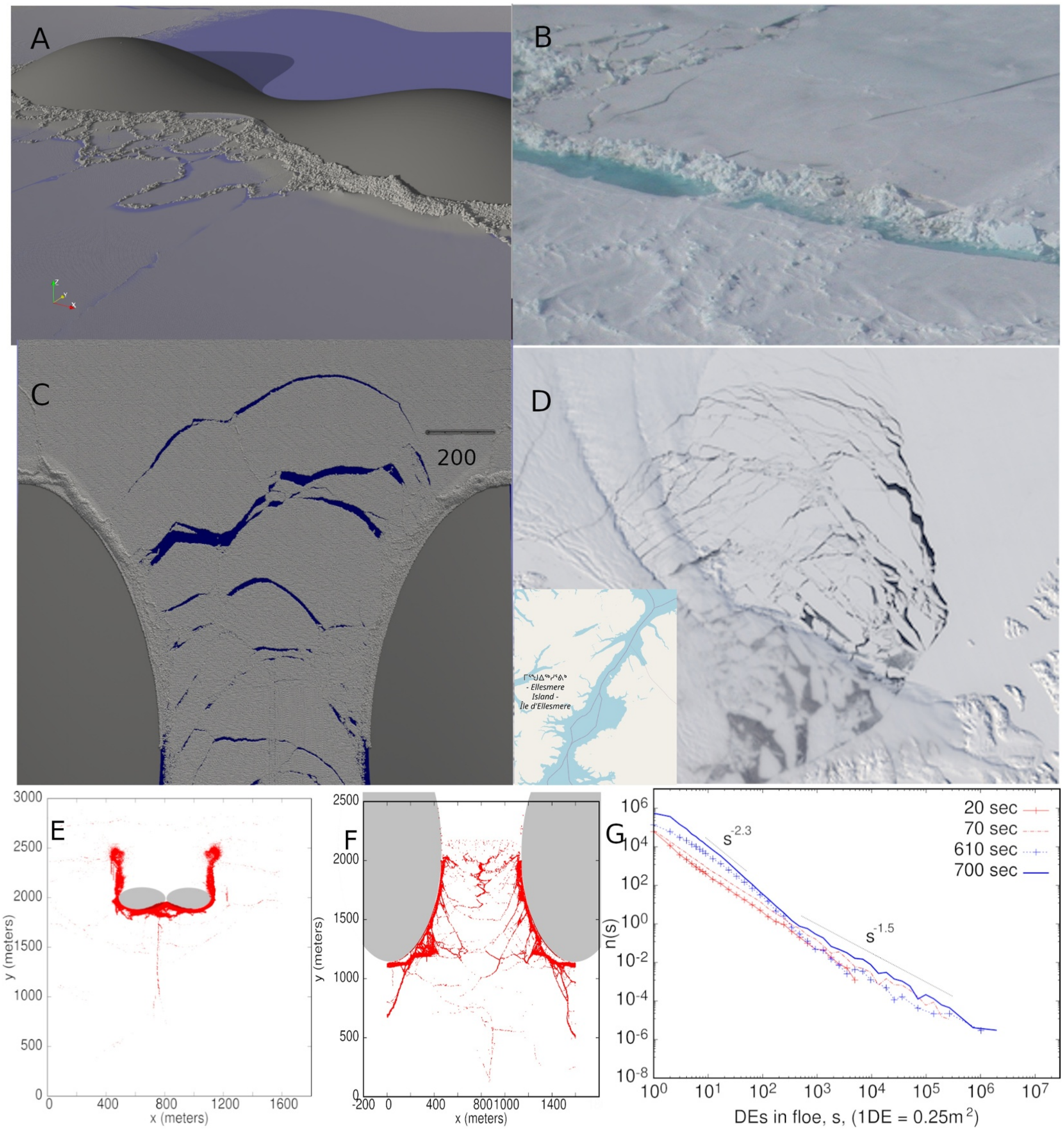

Figure 4. (a) Simulated compression ridges formed when ice is pressed toward a shoreline. Tensile cracks are formed further out from land. Flood water on top of the ice can be seen close to ridges where downwards ice buckling has occurred. (b) A compression ridge photo (NOAA, PMEL Arctic zone (Eicken, 2024)). (c) Ice disintegration as ice is pressed through a narrow strait between two islands. (d) A satellite image of the fragmented ice after the collapse of an ice bridge north of the Nares Strait in may 2017 (NASA Earth Observatory (Voiland, 2017),). The insert (OpenStreetMap) shows Nares Strait between Ellesemere Island and Greenland. (e) Fragments with less than 100 DEs for the island case. (f) Fragments with less than 100 DEs in the strait simulation. (g) The FSDs of the strait and the islands simulations. The early breakup at 20 s (island) and at 70 s (strait), and the late FSDs at 610 (island) and at 700 s (strait).

3.4. Ice Failure Against Shorelines

Finally we investigate two cases when ice is pressed against shorelines: an island, and a narrow strait both modeled by eliptical Gaussian functions. The results are displayed in Figure 4. Figure 4a shows simulated compression ridges formed close to the shore of the island. The highest ridges form right on the shore with ice initially failing due to out-of-plane shear. Further away from the shore, water can be seen on top of the ice right by the ridges. This is a feature often observed at ridge fields as illustrated by an example image in 4b. Even further out there appear a few tensile leads (Figure 4a). Figure 4e displays all fragments with less than 100 DEs. This figure again demonstrates that the most intense fragmentation is located in ridges and that small fragments are also formed within tensile leads.

Figure 4c illustrates the simulation of a strait with ice driven through it from the north. The narrowing of the strait results in compression perpendicular to the direction of ice motion, leading to arching and consequent ice bridges. As the pressure increases, the ice bridges eventually collapse, allowing the ice to pass through the strait. The formation and collapse of ice bridges are distinct features of the ice dynamics in, for example, the Nares Strait (Kwok, 2005) and they affect the outflow of ice from the Arctic Ocean. In addition to ice bridges, pressure ridges form on the windward side of the strait and along the shoreline. A satellite image of the northern end of the Nares Strait following the collapse of an ice bridge event is depicted in Figure 4d. The fragmented ice seen in this image bears a resemblance to the structure observed in the simulations, even though at a much larger scale. The ridges are too small to be observed in satellite images, but the ridge locations modeled in the Nares Strait by Dansereau et al. (2017) are consistent with Figure 4c.

Figures 4e and 4f shows all fragments with less than 100 DEs for the island and the strait simulations. Again the small fragments tend to accumulate in pressure ridges and within the open leads. The FSDs for both the strait (with lines) and the island (with markers) simulations are presented in Figure 4g, both shortly after breakup is initiated and later, when the ice has undergone significant fragmentation. A notable difference in these FSDs compared to the previous ones is that the density of the smaller fragments can no longer be accurately described by the crack-branching function, requiring a much smaller power-law exponent of approximately -2.3. The increased number of small fragments results from the crushing of ice against the coast during the formation of pressure ridges.

4. Discussion

Overall, the FSDs described above align fairly well with those observed in natural settings, typically fitting a single power-law with exponents ranging from -1.65 to -2.03 (Denton & Timmermans, 2022). They also show reasonable agreement with FSDs from simulations by Manucharyan and Montemuro (2022). When compared to field observations, some differences are expected, considering that in natural scenarios, FSDs are rarely extracted immediately after a single fragmentation event. Additionally, the square kilometer areas we have modeled fail due to shear, tension, or compression, while in nature, sea ice fragmentation often results from varying stress conditions over an extended period, emphasizing the importance of post-fracture crushing and grinding that tend to reduce the power-law exponent of observed FSDs. This variation is also evident with HiDEM. When dealing with natural coastlines, larger sizes, and longer simulation times, the code generates FSDs similar to those observed (J. Åström et al., 2024). In these simulations, the minimum floe size was limited to approximately $50m^2$, which matches the resolution in Denton and Timmermans (2022). HiDEM simulations at this resolution, given reasonably accurate initial ice conditions and weather forecasts, are capable of predicting the formation of leads and the rudimentary structure of ridge-networks to a reasonable degree across tens of thousands of square kilometers of ice. This version of HiDEM can thus act as a bridge between the simulations here and continuum models. It is, however, only the half-meter resolution implementation of HiDEM presented here that is capable of modeling ridges, floes and leads in detail. Together they highlight the importance of sea ice dynamics models at different length scales and with varying resolutions.

We have here shown explicitly that the details of sea ice fragmentation depend on the type of external loading leading to ice break-up, and that compression ridges, leads, and drift ice form rather complex structures. The FSDs from the pure shear experiments can be satisfactorily matched by Equation 2. The smaller shear force generates a single lead with floes confined to small sizes within this lead (Figure 1a). The high shear force (Figure 1b) breaks the ice, resulting in an FSD that can be modeled by summing two terms with the form given by Equation 2. The minor fragment aspect of the pure tension FSD can also be matched by Equation 2. The small fragments formed within the large leads are prominently visible in (Figure 2b). For the larger floes, an exponential FSD is appropriate. The same equation, Equation 2, also adequately fits Figures 3a and 4g, except that in these cases, floes resulting from crushing and grinding are also present.

All the detailed features demonstrated here arise from brittle fragmentation and granular interactions. This type of behavior is practically impossible to fully capture with an effective material rheology, as they are inherently discrete in nature, in contrast to continuum models. This suggests that a hybrid model combining DEMs and continuum models may be the best way forward to develop sea ice dynamics forecast models. For creating a hybrid model, it is crucial to align the outcomes from the different models at a 'converging' length scale, specifically around 10 km, where both models are applicable. This involves adjusting the models until the dynamics of the sea ice are reasonably comparable in both, regardless of the loading. It is obviously essential that the results from both models also align with observations.

After aligning a continuum model and a DEM to match each other and observations, an ice dynamics forecast can be conducted by initially generating large-scale results with the continuum model. These results can then provide local stresses to be used as applied stress states for local DEM simulations in areas where detailed predictions of packed and deformed ice formation are necessary. Key applications for such models include assessing the impact wind farms interacting with local ice dynamics, modeling ice behavior in coastal sea regions, and predicting ice conditions along shipping routes and in harbor areas.

Data Availability Statement

A release version of the HiDEM code is available at Todd (2018). The code used here is a beta-version and not yet publicly available.

Acknowledgments
JÅ acknowledges the financial support of the NOCOS-DT project funded by the Nordic Council of Ministers. AP acknowledges the funding from the European Union—NextGenerationEU instrument through Academy of Finland under grant number (348586) WindySea - Modelling engine to design, assess environmental impacts, and operate wind farms for ice-covered waters.

References

Åström, J., Robertsen, F., Haapala, J., Polojärvi, A., Uiboupin, R., & Maljutenko, I. (2024). A large-scale high-resolution numerical model for sea-ice fragmentation dynamics. *The Cryosphere*, *18*(5), 2429–2442. https://doi.org/10.5194/tc-18-2429-2024

Åström, J. A. (2006). Statistical models of brittle fragmentation. *Advances in Physics*, *54*(3–4), 247–278. https://doi.org/10.1080/00018730600731907

Babic, M., Shen, H., & Bedov, G. (1990). Discrete element simulations of river ice transport. *InProc.of the 12th IAHR Int. Symposium on Ice*, *1*, 564–574.

Benn, D. I., & Åström, J. A. (2018). Calving glaciers and ice shelves. *Advances in Physics X*, *3*(1), 1513819. https://doi.org/10.1080/23746149.2018.1513819

Benn, D. I., Luckman, A., Åström, J. A., Crawford, A. J., Cornford, S. L., Bevan, S. L., et al. (2022). Rapid fragmentation of thwaites eastern ice shelf. *The Cryosphere*, *16*(6), 2545–2564. https://doi.org/10.5194/tc-16-2545-2022

Blockley, F. e. a. (2020). The future of sea ice modelling. toward defining a cutting-edge future for sea ice modelling. *Bulletin of American Meterological Society*, E1304.

Bouchat, A., Hutter, N., Chanut, J., Dupont, F., Dukhovskoy, D., Garric, G., et al. (2022). A ice rheology experiment (sirex): 1. scaling and statistical properties of sea-ice deformation fields. *Journal of Geophysical Research: Oceans*, *127*(4). https://doi.org/10.1029/2021JC017667

Cundall, P., & Strack, O. (1979). A discrete numerical model for granular assemblies. *Géotechnique*, *29*(1), 47–65. https://doi.org/10.1680/geot.1979.29.1.47

Dansereau, V., Weis, J., Saramito, P., & Lattes, P. (2016). A Maxwell elasto-brittle rheology for sea ice modelling. *The Cryosphere*, *10*(3), 1339–1359. https://doi.org/10.5194/tc-10-1339-2016

Dansereau, V., Weiss, J., Saramito, P., Lattes, P., & Coche, E. (2017). Ice bridges and ridges in the maxwell-eb sea ice rheology. *The Cryosphere*, *11*(5), 2033–2058. https://doi.org/10.5194/tc-11-2033-2017

Denton, A. A., & Timmermans, M.-L. (2022). Characterizing the sea-ice floe size distribution in the Canada basin from high-resolution optical satellite imagery. *The Cryosphere*, *16*(5), 1563–1578. https://doi.org/10.5194/tc-16-1563-2022

Eicken, H. (2024). What is the difference between rubble ice and pressure ridges? Retrieved from https://www.pmel.noaa.gov/arctic-zone/ice-rubble-pressure.html

Feltham, D. (2008). Sea ice rheology. *Annual Review of Fluid Mechanics*, *40*(1), 91–112. https://doi.org/10.1146/annurev.fluid.40.111406.102151

Grady, D., & Kipp, M. (1985). Geometric statistics and dynamic fragmentation. *Journal of Applied Physics*, *58*(3), 1210–1222. https://doi.org/10.1063/1.336139

Herman, A. (2022). Granular effects in sea ice rheology in the marginal ice zone. *Philosophical Transactions of the Royal Society A: Mathematical, Physical & Engineering Sciences*, *380*(2235). https://doi.org/10.1098/rsta.2021.0260

Hibler, W. (1977). A viscous sea ice law as a stochastic average of plasticity. *Journal of Geophysical Research*, *82*(27), 3932–3938. https://doi.org/10.1029/jc082i027p03932

Hibler, W. (1979). A dynamic thermodynamic sea ice model. *Journal of Physical Oceanography*, *9*(4), 815–846. https://doi.org/10.1175/1520-0485(1979)009<0815:adtsim>2.0.co;2

Hopkins, M. (1994). On the ridging of intact lead ice. *Journal of Geophysical Research*, *99*(C8), 16351–16360. https://doi.org/10.1029/94jc00996

Hopkins, M. (1996). On the mesoscale interaction of lead ice and floes. *Journal of Geophysical Research*, *101*(C8), 315–326. https://doi.org/10.1029/96JC01689

Hopkins, M. (1998). Four stages of pressure ridging. *Journal of Geophysical Research*, *103*(C10), 21883–21891. https://doi.org/10.1029/98jc01257

Hopkins, M., Frankenstein, S., & Thorndike, A. S. (2004). Formation of an aggregate scale in arctic sea ice. *Journal of Geophysical Research*, *109*(1), C01032. https://doi.org/10.1029/2003jc001855

Hopkins, M., & Hibler, I. W. (1991). Numerical simulations of a compact convergent system of ice floes. *Annals of Glaciology*, *15*, 26–30. https://doi.org/10.3189/1991aog15-1-26-30

Hopkins, M., Hibler, W., & Flato, G. (1991). On the numerical simulation of the sea ice ridging process. *Journal of Geophysical Research*, *96*(C3), 4809–4820. https://doi.org/10.1029/90jc02375

Hopkins, M., & Thorndike, A. S. (2006). Floe formation in arctic sea ice. *Journal of Geophysical Research*, *111*(C11). https://doi.org/10.1029/2005jc003352

Hopkins, M., Tuhkuri, J., & Lensu, M. (1999). Rafting and ridging of thin ice sheets. *Journal of Geophysical Research*, *104*(C6), 13605–13613. https://doi.org/10.1029/1999jc900031

Hutter, N., Bouchat, A., Dupont, F., Dukhovskoy, D., Koldunov, N., Lee, Y. J., et al. (2022). Sea ice rheology experiment (sirex): 2. Evaluating linear kinematic features in high-resolution sea ice simulations. *Journal of Geophysical Research*, *127*(4). https://doi.org/10.1029/2021JC017666

Iravani, A., Åström, J. A., & Ouchterlony, F. (2018). Physical origin of the fine-particle problem in blasting fragmentation. *Physical Review Applied*, *10*(3), 034001. https://doi.org/10.1103/physrevapplied.10.034001

Kärnä, T., Ljungemyr, P., Falahat, S., Ringgaard, I., Axell, L., Korabel, V., et al. (2021). Nemo-nordic 2.0: Operational marine forecast model for the baltic sea. *Geoscientific Model Development*, *14*(9), 5731–5749. https://doi.org/10.5194/gmd-14-5731-2021

Kwok, R. (2005). Variability of nares strait ice flux. *Geophysical Research Letters*, *32*(24), L24502. https://doi.org/10.1029/2005GL024768

Manna, S. S., & Herrmann, H. J. (1991). Precise determination of the fractal dimensions of apollonian packing and space-filling bearings. *Journal of Physics A: Mathematical and General*, *24*(9), 481–490. https://doi.org/10.1088/0305-4470/24/9/006

Manucharyan, G. E., & Montemuro, B. P. (2022). Subzero: A sea ice model with an explicit representation of the floe life cycle. *Journal of Advances in Modeling Earth Systems*, *14*(12), e2022MS003247. https://doi.org/10.1029/2022ms003247

Marbouti, M., Eriksson, L., Dammann, D. O., Demchev, D., Jones, J., Berg, A., & Antropov, O. (2020). Evaluating landfast sea ice ridging near utqiavik Alaska using tandem-x interferometry. *Remote Sensing*, *12*(8), 1247. https://doi.org/10.3390/rs12081247

Ólason, E., Boutin, G., Korosov, A., Rampal, P., Williams, T., Kimmritz, M., et al. (2022). A new brittle rheology and numerical framework for large-scale sea-ice models. *Journal of Advances in Modeling Earth Systems*, *14*, 8. https://doi.org/10.1029/2021ms002685

Pemberton, P., Löptien, U., Hordoir, R., Höglund, A., Schimanke, S., Axell, L., & Haapala, J. (2017). Sea-Ice evaluation of nemo-nordic 1.0: A nemo–lim3.6-based ocean–sea-ice model setup for the north sea and baltic sea. *Geoscientific Model Development*, *10*(8), 3105–3123. https://doi.org/10.5194/gmd-10-3105-2017

Prasanna, M., Polojärvi, A., Wei, M., & Åström, J. (2022). Modeling ice block failure within drift ice and ice rubble. *Physical Review A*, *105*(4), 045001. https://doi.org/10.1103/PhysRevE.105.045001

Rheinlænder, J. W., Davy, R., Ólason, E., Rampal, P., Spensberger, C., Williams, T. D., et al. (2022). Driving mechanisms of an extreme winter sea ice breakup event in the beaufort sea. *Geophysical Research Letters*, *49*(12), e2022GL099024. https://doi.org/10.1029/2022gl099024

Röhrs, J., Gusdal, Y., Rikardsen, E., Duran Moro, M., Brændshøi, J., Kristensen, N. M., et al. (2023). Barents-2.5km v2.0: An operational data-assimilative coupled ocean and sea ice ensemble prediction model for the barents sea and svalbard. *Geoscientific Model Development Discussions*. https://doi.org/10.5194/gmd-2023-20

Schreyer, H., Sulsky, D., Munday, L., Coon, M., & Kwok, R. (2006). Elastic-decohesive constitutive model for sea ice. *Journal of Geophysical Research*, *111*(C11), C11526. https://doi.org/10.1029/2005jc003334

Todd, J. (2018). joeatodd/hidem: Initial release of hidem (v1.0). *Zenodo*. https://doi.org/10.5281/zenodo.1252379

Voiland, A. (2017). Breakdown of an ice arch. *NASA Earth Observatory image by Jesse Allen, data from the Land Atmosphere Near real-time Capability for EOS (LANCE)*. Retrieved from https://earthobservatory.nasa.gov/images/90245/breakdown-of-an-ice-arch?src=ve

West, B., O'Connor, D., Parno, M., Krackow, M., & Polashenski, C. (2022). Bonded discrete element simulations of sea ice with non-local failure, applications to nares strait. *Journal of Advances in Modeling Earth Systems*, *14*(6), e2021MS002614. https://doi.org/10.1029/2021ms002614